Simulation and Validation Studies of a Large Drift Tube Muon Tracker

Guangliang Yang[a], Josh Schoetker[b], Dan Poulson[c], Elena Guardincerri[c], J.M. Durham[c], Sven Vogel[c], Shaun Hoerner[d], Derek Aberle[c], Ke-Xun Sun[b], C. L. Morris[c], Ralf Kaiser[a], Andrew Osborne[d,e•]

[a]*Nuclear and Hadron Physics Group, University of Glasgow, Kelvin Building, University Avenue, Glasgow G12 8QQ, Scotland, UK*

[b]*University of Nevada Las Vegas, Las Vegas, NV 89154, USA*

[c]*Los Alamos National Laboratory, Los Alamos, NM 87545, USA*

[d]*Department of Mechanical Engineering, The Colorado School of Mines, 1610 Illinois St., Golden, CO, 80401, USA*

[e]*Nuclear Science & Engineering, The Colorado School of Mines, 1012 14th St., Golden, CO, 80401, USA*

Abstract. Cosmic ray muons are massive, charged particles created from high energy cosmic rays colliding with atomic nuclei in Earth's atmosphere. Because of their high momenta and weak interaction, these muons can penetrate through large thicknesses of dense material before being absorbed, making them ideal for nondestructive imaging of objects composed of high-Z elements. A Giant Muon Tracker with two horizontal 8'×6' and two vertical 6×6' modules of drift tubes was used to measure muon tracks passing through samples placed inside the detector volume. The experimental results were used to validate a Monte Carlo simulation of the Giant Muon Tracker. Imaging results of simulated samples were reconstructed and compared with those from the experiment and showed excellent agreement.

Keywords: GEANT4, cosmic ray muons

•**Corresponding author.** Email: osbornea@mines.edu.

1. Introduction. Cosmic ray muons are charged particles with masses 205 times that of electrons, created from cosmic ray interactions with nuclei in Earth's atmosphere. Because the distribution of these muons' energies has an average energy at around 4 GeV [1] and weak interaction, they can be ideal for nondestructive imaging of thick, dense objects. The flux of cosmic ray muons at sea level, however, is only approximately 1 muon/cm^2/min. Consequently, muon detectors with large surface areas are typically used with long exposure times to perform imaging. Cosmic ray muons have been used in a variety of contexts, including geological mapping of volcanos [2] and underground tunnels [3]. These kinds of studies demonstrate the suitability of cosmic ray muons for performing imaging underneath dense media through which X-ray or gamma radiation would not penetrate [4]–[6]. Cosmic ray muography has also been shown to have utility in imaging structural components of historic buildings [7], nuclear reactors [8], and in power industry applications [9]. Simulation and experimental studies in recent years [10]–[13] have shown that cosmic ray muography also has significant potential for monitoring the interior of spent

nuclear fuel casks. Cosmic ray imaging has also been investigated as a method for border security and cargo inspection [14]–[16], a key objective of which is to detect special nuclear material. Detailed reviews of principles and applications of cosmic ray muon imaging are given in [16]–[18].

Many of the past studies in cosmic ray imaging were performed at the Los Alamos National Laboratory (LANL) using a Medium Muon Tracker (MMT). The MMT consists of two modules of drift tubes with dimensions of 4'×4' [3], [7], [9], [10]. Each module contains submodules with layers of perpendicular drift tubes to enable the reconstruction of positions on detector planes where muon tracks underwent interactions. A much larger detector, the Giant Muon Tracker (GMT) was recently commissioned at LANL for use primarily in spent nuclear fuel cask inspection. The GMT consists of four drift tube supermodules with dimensions 6'×6' and 6'×8'. In this work we describe the experimental measurements taken with the GMT for imaging a range of samples in a variety of geometric configurations for the first time. Samples' material compositions included polyethylene, aluminum, wood, steel, copper, brass, acrylic, concrete and lead. We also detail the development of a Geant4 [19] simulation of the GMT and perform validation and verification of the simulation model using the experimental results. We show that the simulation model reproduces the performance of the GMT with high accuracy.

2. Methods.

2.1. Giant Muon Tracker (GMT). The tracker consists of four supermodules of drift tubes arranged in the configuration shown in Fig. 1. Although in this work the position of each supermodule is fixed, each supermodule can be moved independently. Each supermodule consists of layers of drift tubes arranged in three modules of two pairs of layers. Layers of drift tubes in a pair are staggered, and each pair is followed by another pair of layers oriented orthogonally to the other in a module. This arrangement enables muon track intersections' spatial locations to be reconstructed in each module. Multiple modules improve the accuracy of reconstruction. The two vertical supermodules each have dimensions of 190.26×190.26×57.68 cm and consist of 432 drift tubes. The larger horizontal supermodules each have dimensions of 190.26×251.52×57.64 cm and consist of 504 drift tubes. Figure 2 shows a photograph of the assembled GMT at the LANSCE experimental staging area at Los Alamos National Laboratory.

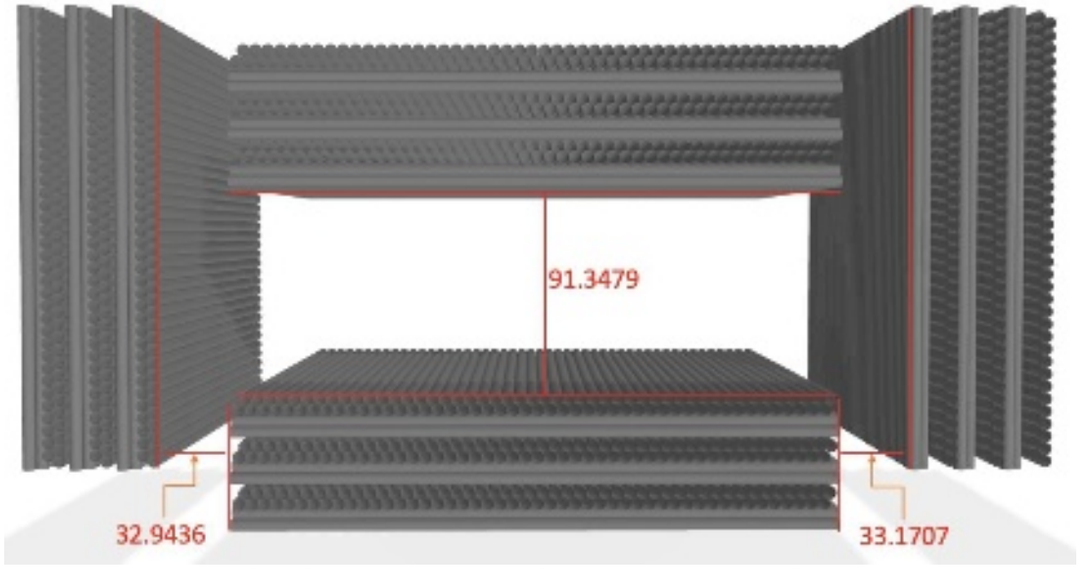

Figure 1. CAD Rendered Giant Muon Tracker. Dimensions are shown in centimeters. The configuration shown reflects the present setup at the Los Alamos National Laboratory and was used to take the data for this work. Samples were placed in the central space between supermodules.

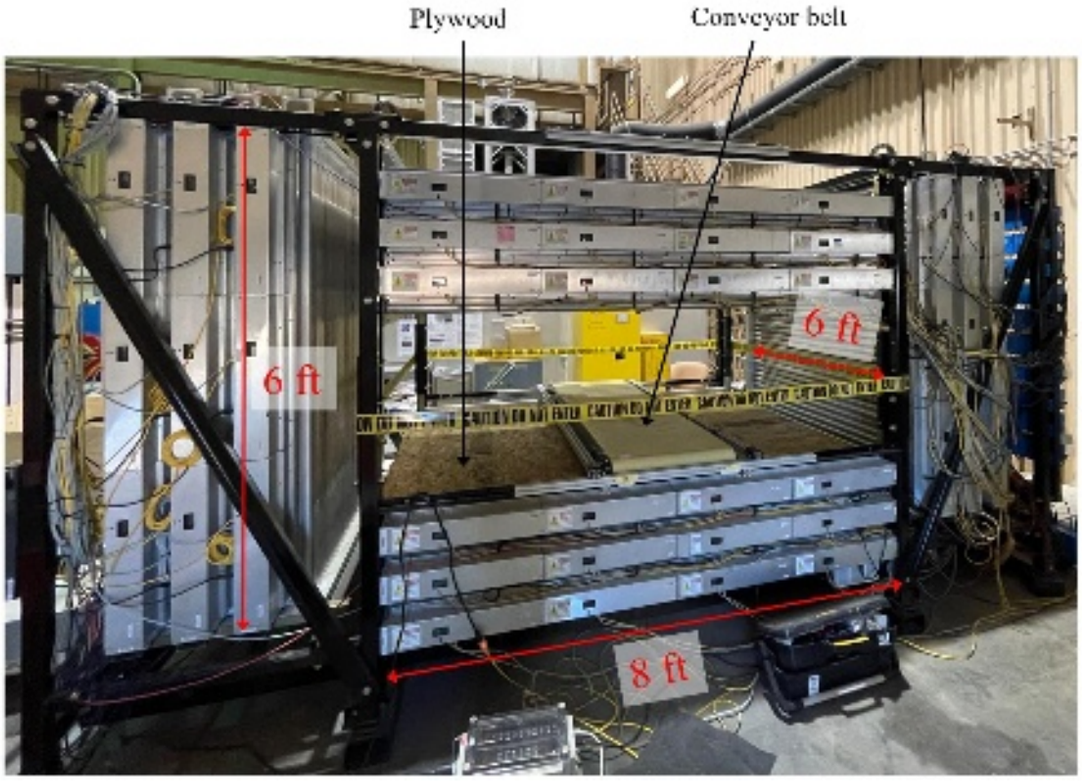

Figure 2. Assembled Giant Muon Tracker. Plywood boards were placed above the lower supermodule to protect the drift tubes from damage during sample placement. A conveyor belt is included for holding and moving heavy samples. The conveyor belt is mounted to the steel frame using aluminum T-Slot rails.

2.2 Drift Tubes. Drift tubes are either 1.8 m or 2.4 m in length, and all have an outer radius and wall thickness of 5.08 cm and 0.9 mm respectively, Fig. 3. The drift tubes are weld sealed on both ends with aluminum end-caps and have a 30 μm, gold-plated tungsten anode wire that runs along the tube axis. A gas mixture of 47.5% Ar, 42.5% CF_4, and 7.5% C_2H_6, and 2.5% He with a pressure of 1 bar fills the tubes. During operation for this work, the tubes' anode wires were biased at a voltage of +2650 V relative to the aluminum wall. The ionization of the tube gas by the passage of a cosmic-ray muon is amplified as the liberated electrons drift to the anode wire, resulting in a measurable voltage pulse.

Figure 3. Laboratory Test Drift Tube. The GMT consists of drift tubes similar to the pictured test drift tube. Differences are length (1.8 or 2.4m in the GMT), and end connections for compatibility with GMT sockets.

2.3 Readout Electronics. Custom readout electronics for the GMT were developed and manufactured by Decision Sciences (https://www.decisionsciences.com/). The readout electronics are composed of three printed circuit boards (PCBs). The first PCB provides bias, AC signal pickoff, and charge sensitive amplification for 24 tubes. Following signal amplification, multi-threshold discriminators convert the analog signal into a series of logic pulses. The second PCB houses a field-programmable gate array (FPGA) that handles a global 200 MHz clock signal via a master/slave synchronization pulse. The second PCB also performs time-to-digital (TDC) time stamping of the discriminator logic pulses and exports the TDC buffers to the data acquisition (DAQ) system at 1 second intervals. The top PCB handles DAQ communication and clock synchronization signals via two Ethernet ports.

2.4 Data Acquisition System and Track Reconstruction. Each GMT module that is read out by an FPGA is synchronized in time by a slave/master clock system. All FPGAs export their TDC buffers to the DAQ system at 1 second intervals. The DAQ system is triggerless and uses temporal coincidence windows to group the measured hits in the GMT drift tubes. Once grouped, Least Absolute Deviation [20] regression is used to suppress outliers and determine the best fit muon track within a GMT supermodule. The track fitting is composed of two independent fits, one for each set of parallel drift tubes within a supermodule. The initial fit is performed using the anode position within each hit tube to create an approximate muon track in the supermodule. Subsequently, the coarse fit is refined by taking into account the TDC and drift velocity data for each tube to arrive at a best fit muon track.

When two GMT supermodules produce tracks that are temporally coincident, the tracks are assumed to be the result of a scattered incident muon and its exiting track after passing between the supermodules. If a single incident track is produced with a directional vector such that an exiting track is expected but not observed, then it is assumed that the muon was stopped between the supermodules. Scattered and stopped muon tracks are separately recorded for use in scattering and transmission tomography analysis.

2.5. Muon Imaging. Charged particle multiple scattering has been studied extensively in the past century with Molière [21], Goudsmit and Saunderson [22] and Lewis [23] providing the most important foundational contributions. According to Molière's theory, the angular distribution in multiple scattering can be approximated as a heavy-tailed distribution. The central Gaussian shape of the distribution is caused by many small angle scatters, while the heavy tail is caused by large single scatters. Although the width of the distribution can be estimated accurately by using Molière's theory, the calculation is computationally expensive. Because of this, Rossi and Greisen [24] developed a simple approximation to Molière's theory by fitting a Gaussian distribution to Molière's multiple scattering distribution, Eq. (1):

$$\sigma = \frac{14.1MeV}{pv}\sqrt{\frac{t}{X}} \tag{1}.$$

Here σ is the standard deviation of the distribution, p is the momentum of the particle [MeV] and v is its speed. The symbols t and X represent the thickness of the medium in the direction of travel and its radiation length, both with units of length. The radiation length is characteristic of the medium in which the particle scatters and can be approximated according to Eq. (2) [25]:

$$X = \frac{716.4gcm^{-2}A}{\rho Z(Z+1)\ln\left(\frac{287}{\sqrt{Z}}\right)} \tag{2}.$$

In Eq. (2) the symbols A, Z and ρ refer to the atomic mass, atomic number and density of the material. Equations (1) and (2) are applicable to a single layer of homogeneous material. In tomographic problems a heterogeneous material can be approximated as many layers of materials with different radiation lengths. A first order approximation of the variance in the scattering angle distribution through multiple layers can be calculated by adding the variance of individual layers, Eq. (3):

$$\sigma^2 = \sum_i \left(\frac{14.1MeV}{p_i v_i}\right)^2 \frac{t_i}{X_i} \tag{3}$$

where t_i, X_i are the thickness and radiation length of layer i. The symbols p_i and v_i are the particle momenta [MeV] and speed in layer i. In image reconstruction for multiple scattering tomography the scattering angle distributions are measured, while the radiation lengths X_i describing each material are sought. This inverse problem can be solved after developing a formulation for the angular scattering distribution from a voxelated medium using Eq. (3) as a basis. A particle that moves along a specific path k can experience single or multiple scattering in each voxel i through which it travels. Equation (4) expresses the variance in the scattering distribution that is developed as the particle travels:

$$\sigma_k{}^2 = \sum_i \left(\frac{14.1MeV}{p_k v_k}\right)^2 t_{ik}\lambda_i \quad (4).$$

Here the symbol $\lambda_i = 1/X_i$ is used for simplification and t_{ik} is the path length inside the voxel through which the muon travels. Importantly, Eq. (4) is given under the assumption that the particle's energy loss inside the material is zero. This is done because the momenta of muons as they enter and leave voxels are not measurable in most situations. This assumption, however, can be accommodated by assuming that for a given muon path k, the momentum distribution of the muon $f(p)$ is independent of direction. For a fixed momentum the scattering angle follows an approximately Gaussian distribution, and it can be shown that the mean variance of the scattering angle is given by Eq. (5):

$$\langle\sigma^2\rangle = \int_0^\infty \sigma^2 f(p)dp \quad (5).$$

Substituting Eq. (4) into Eq. (5) and integrating over momentum gives:

$$\langle\sigma^2\rangle = \sum_i t_{ik}\tilde{\lambda}_i \quad (6)$$

where the effective scattering density $\tilde{\lambda} = q\lambda$ and

$$q = \langle\frac{(14.1MeV)^2}{p^2v^2}\rangle \quad (7).$$

Equation (6) is more practical in cosmic ray muon tomography because the factor q, Eq. (7), cannot always be calculated since the muon momentum is typically not known. In image reconstruction, however, only the contrast between voxels is needed to discriminate between materials in a sample. Because of this, none of the quantities in Eq. (7) need to be known and solving for $\tilde{\lambda}_i$ in Eq. (6) as an inverse problem is sufficient. The mean variance in the scattering angle $\langle\sigma^2\rangle$ is calculated using incoming and outgoing muon track vectors as measured by the imaging system.

2.6. Monte Carlo Simulations. Simulations were done using the Geant4 toolkit [19] coupled with the ROOT analysis framework [26]. A muon source was generated using the CRY code [27] with energy and angle distributions at sea level and 2100m shown in Fig. 4. The 2100m distributions are the closest available in CRY to the 2230m altitude of Los Alamos, NM, where the experiments took place. Muon interactions with materials in Geant4 are simulated using the Wentzel-VI Combined Scattering Model for electromagnetic interactions [28], [29].

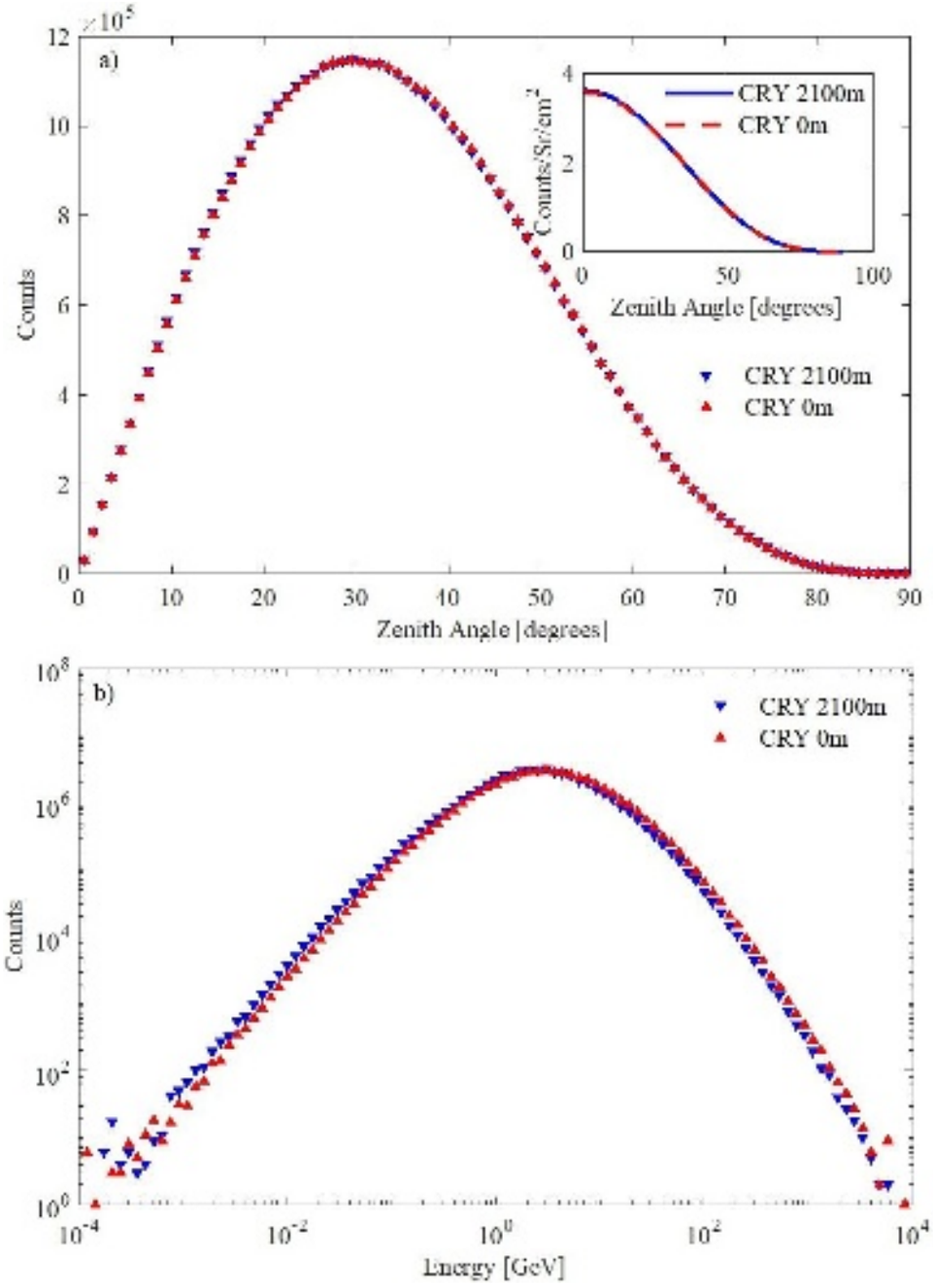

Figure 4. Cosmic ray muon angle (a) and energy (b) distributions. Red and blue points represent distributions at 0 and 2100m altitude respectively, and at a latitude of 35.88° N. The muons' angle distribution can be approximated by $cos^2(\theta)sin(\theta)$. Inset in plot a) shows the muons' angle distribution per unit solid angle.

The drift radius is the distance of closest approach between muon tracks and the central anode wire as the muon travels through a drift tube. While muon tracks can be reconstructed from experimental drift radius measurements, secondary electrons (delta rays) produced by muons' interactions with electrons in the detector gas also deposit energy in the drift tube gas. Consequently, the drift radii of secondary particles also need to be simulated to model the experiment with high fidelity. Unlike muons, secondary electrons can have very small momenta which causes multiple

scattering to have significant effects on their trajectories. Simulating all secondary particles, however, is computationally inefficient because at low momenta the differential cross section of their production rapidly increases. Production cuts are used in Geant4 to limit secondary particle production, and by default their production is simulated only when the expected range of the secondary is at least 1mm. To accurately compute secondary particles' drift radii, their tracks were simulated at high resolution in Geant4 using a production cut of 0.01mm. This value was determined by computing the standard deviation of the muon scattering angle distribution for the whole detector as the production cut was systematically reduced. The standard deviation remains the same to four significant figures when the production cut is decreased from 0.01mm to 0.001mm, while the simulation runtime increases by up to a factor of 10. The geometry of the Giant Muon Tracker was modeled as shown in Fig. 5, at the level of individual, idealized drift tubes consisting of a metal cylinder and central anode wire.

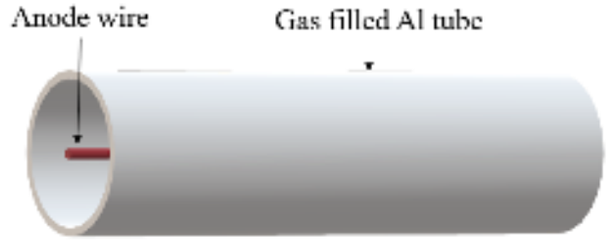

Figure 5. Simulated Drift Tube. The GMT was modeled in Geant4 as planes consisting of idealized drift tubes. Each tube was modeled as a gas filled aluminum cylinder with an anode wire in its center.

The most important effects that contribute to uncertainties in experimental measurements of muon tracks are multiple scattering of muons, delta rays, and drift radius uncertainties. Multiple scattering occurs when muons interact with the materials that are present in the detector itself, and this happens primarily in the drift tube walls. Delta rays caused by muons colliding with atoms in drift tube materials have high enough energies to ionize the drift tube gas, causing electron and ion pairs to register as spurious hits. Approximately 10% of muon hits on a drift tube will be accompanied by delta rays, causing significant uncertainties in the detector resolution. These processes were explicitly simulated using Geant4. Uncertainties associated with drift radius measurements, however, originate from multiple factors. These include uncertainties in electronics' delay time, variances in drift tubes' responses due to calibration drift and manufacturing imperfections, and several others. Rather than attempting to model each contribution to uncertainty explicitly, each recorded drift radius was simply smeared with a Gaussian error in a post-processing step. In order to ensure the Geant4 simulation could accurately model the resulting uncertainties, the variance of the Gaussian error was determined using an iterative approach. The experimentally measured scattering angle distribution is shown in Fig. 6, alongside simulated results with sources of uncertainty included incrementally.

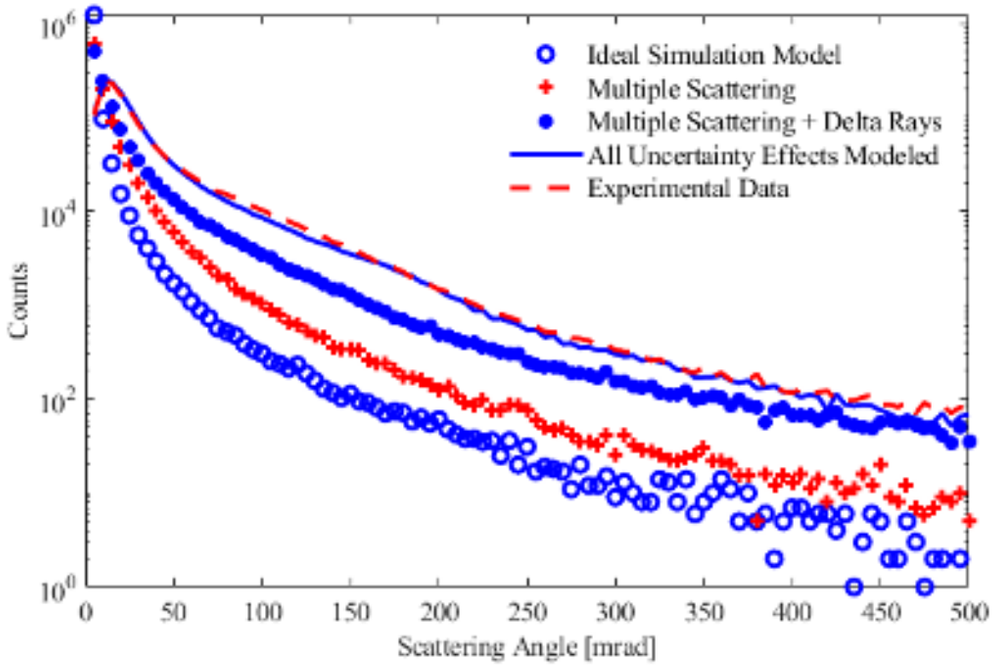

Figure 6. Cosmic ray muon scattering angle distributions. The unfilled blue circles represent the ideal simulation model, while the red dashed curve represents the experimental data. The red crosses represent simulated results with multiple scattering modeled, while the filled blue circles represent simulated results with both multiple scattering and delta ray effects modeled. The solid blue curve shows simulated results with all sources of uncertainty modeled, including drift radius uncertainty. Data are shown for Scan 1, described in Section 3 of this work.

The variance of the Gaussian error was found by minimizing the distance between the scattering angle distribution simulated with all sources of uncertainty and the experimental result. These are represented by the solid blue (simulated) and dashed red (experimental) curves in Fig. 6. A single value of the variance was applied to all simulated drift radii globally.

2.7. Image Reconstruction

Muon tomography images were reconstructed using the Back Projection and Filtering (BPF) algorithm [30] and the Point of Closest Approach (PoCA) method [31] for comparison and initial estimate. In the PoCA method, the point of closest approach between the incoming muon track measured by one scanner supermodule, and the outgoing track measured by the other supermodule is determined. The imaging volume is divided into voxels, each of which records the PoCA that falls inside its boundaries. For each voxel, the median value of the scattering angle is calculated and used to characterize the material inside the voxel. To minimize statistical artifacts, for every PoCA point calculated using the incoming and outgoing muon trajectories, 10 randomly selected alternative PoCA points were calculated. The alternative points are drawn from a Gaussian distribution about the selected point, whose variance is defined by the distance of closest approach between the incoming and outgoing tracks. The distance between the alternative PoCAs and the original follows a Gaussian distribution whose variance is inversely proportional to the scattering angle.

The BPF method is a refinement of the PoCA algorithm, whose first step is to back project the variance of the multiple scattering angle along the muon path. Since the true muon path is not known, a path is initially estimated using the PoCA method. The average of the variance of the scattering angle in each of the voxels in the imaging area forms a simple back projection image. This image is the convolution of the true image with a point spread function. The second step is to deconvolve the simple back projection image using a Fourier transform method.

3. Results

Five experiments were done with the GMT at LANL, one with an empty tracker for a background reading, and four with samples arranged in multiple configurations. The experimental samples' geometry, material compositions and positions were also modeled explicitly in the simulations. Simulations were run on the University of Glasgow Nuclear Group high performance computing cluster. In all Scans, measurements were taken using the GMT for a minimum of 48 hours. During initial testing it was discovered that the DAQ was subject to occasional faults during a run, interrupting data taking. It was determined that 48 hours was the minimum wall-clock data taking time that gave acceptable image quality for developing our simulation model. In each Scan this was split over 4 or more runs and allowed us to accumulate enough track data for accurate imaging while accounting for unpredictable faults. Data taking time and track counts for all Scans are summarized in Table I.

Table I. Experimental Scan summaries.

Scan	Wall-clock time[a] [hours]	Tracks recorded[b] [millions]	Tracks used in imaging[c] [millions]
Empty Scan	48	31	31
Scan 1	63	60	60
Scan 2	92	90	60
Scan 3	80	50	50
Scan 4	54	41	41

a) Actual imaging time was typically less than wall-clock time due to faults in the DAQ causing interruptions in data taking.
b) Tracks recorded refer to full, complete tracks.
c) Imaging here refers to images reconstructed using GMT data and not simulated tracks.

In all Scans using simulated data, image reconstruction was done with done with 60 million tracks. In all simulated and experimental scans, image reconstruction using the BPF and PoCA algorithms were done with voxels of dimensions 0.522 × 1.247 × 1.095 cm (x,y,z). Figure 7 shows the sample geometry and imaging results of Scan 1 in which 11 materials were scanned by the GMT. The simulated and experimental imaging results agree well with each other for high density and high atomic number objects such as steel, copper, lead, concrete and aluminum. For low density and low atomic number objects such as wood and polyethylene there is a more significant contrast between simulated and experimental results. The acrylic is invisible in both cases.

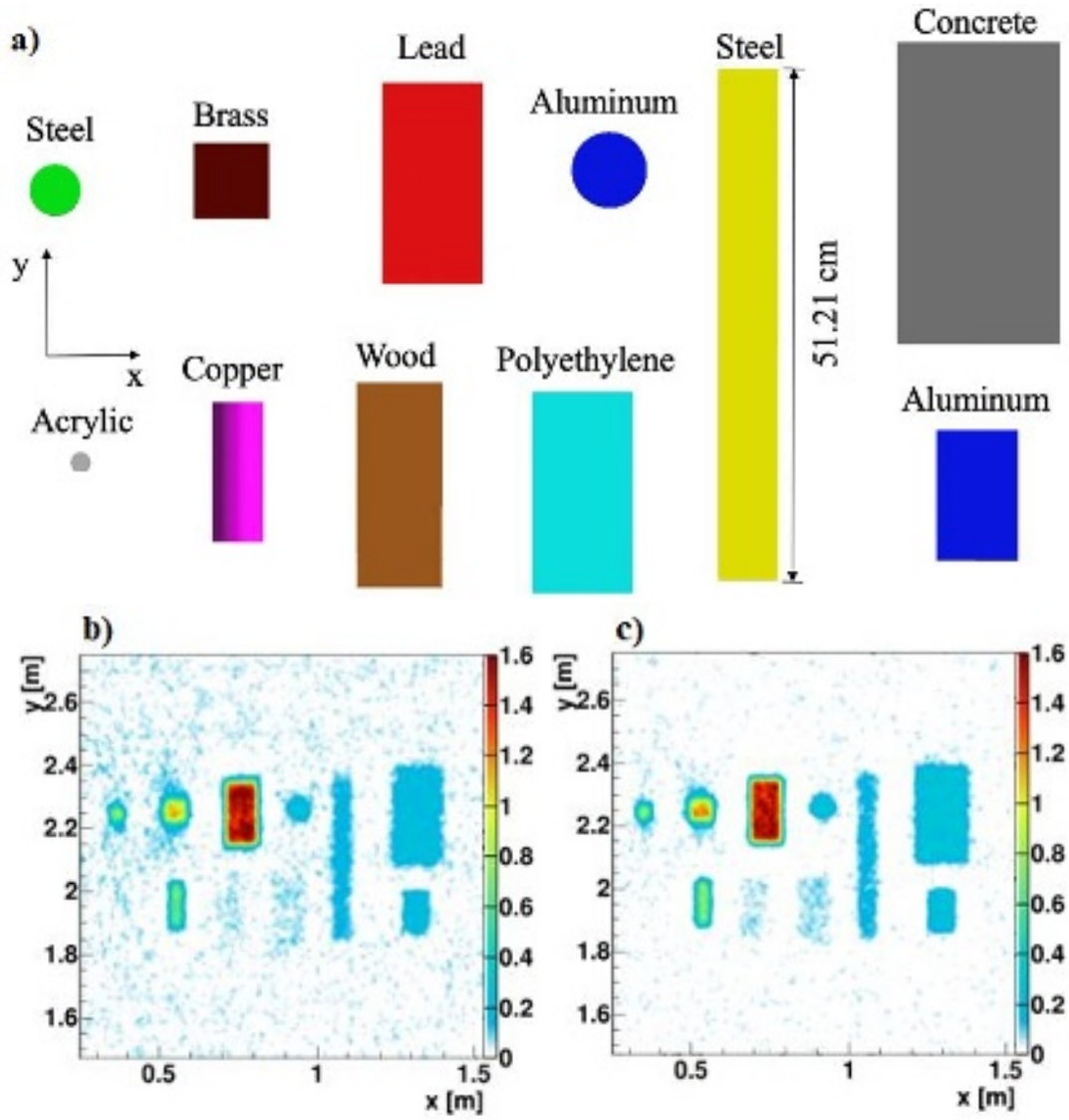

Figure 7. Scan 1 sample geometry and imaging results. (a) CAD rendering of sample geometry, top-down aspect. Lead, wood, polyethylene, concrete and rightmost aluminum samples are cuboids, while copper sample is a cylinder. Steel, acrylic and aluminum samples that appear as circles are spheres. (b) image reconstruction, experimental GMT scan. (c) Simulated scan. Imaging volume is a 6cm thick slice whose bottom is coincident with the surface of a 49mm foam layer placed on the conveyor belt. Images shown were reconstructed using BPF algorithm.

Figure 8 shows the sample geometry and horizontal plane imaging results of Scan 2. While the samples of Scan 1 consisted entirely of solid objects, the Scan 2 samples were arranged to incorporate voids between solid materials. Scan 2 samples also included a polyethylene block between brass plates and angled bricks of aluminum. Figure 9 shows the reconstructed image of the isolated lead bricks in Sample 2, in the vertical plane. The vertical separation between bricks is 4.9 cm, low enough for the GMT to have difficulty in resolving with the given statistics, and this limitation is reflected in the simulated data. In all cases the experimental and simulated imaging results agreed well with each other.

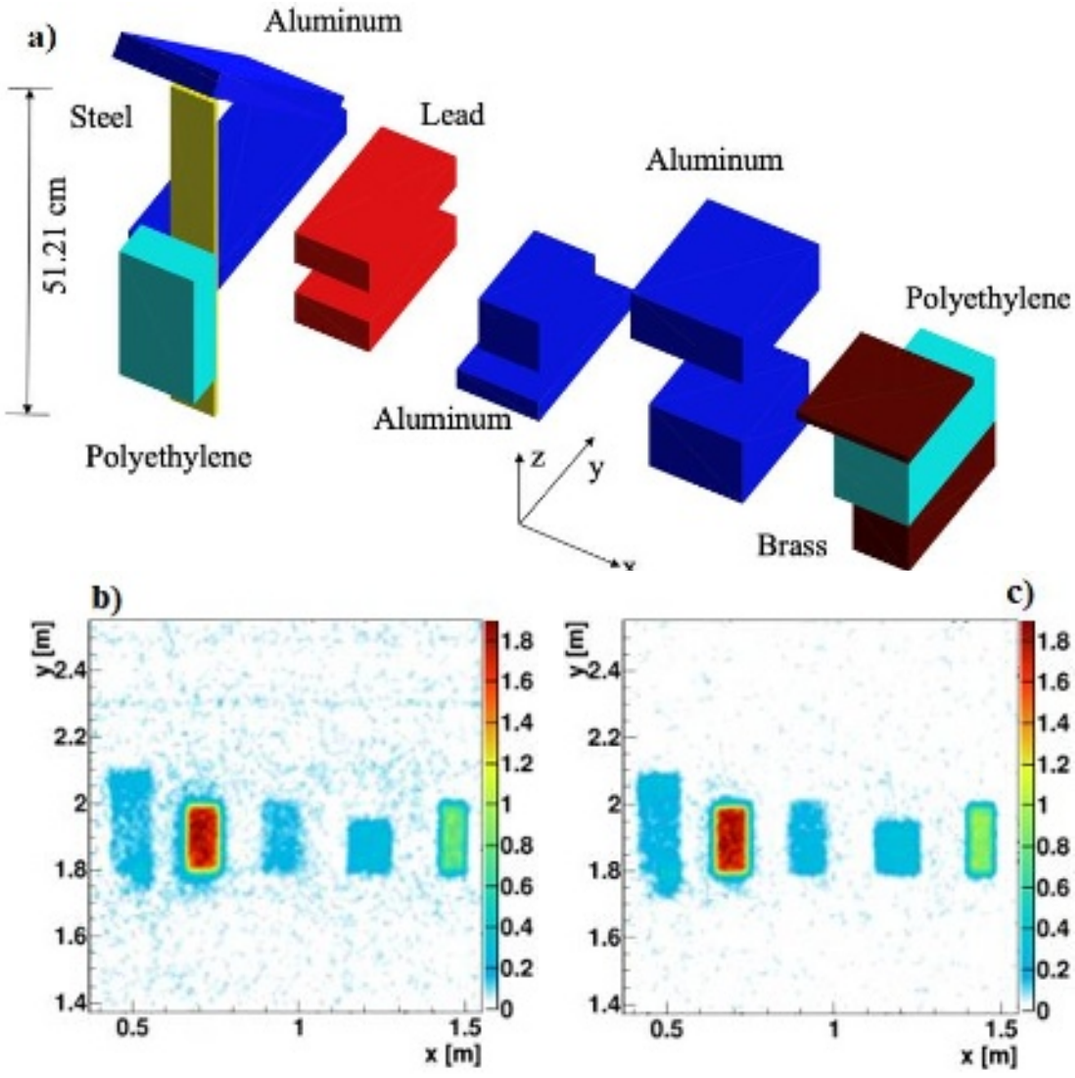

Figure 8. Scan 2 sample geometry and imaging results. (a) CAD rendering of sample geometry. Pairs of lead blocks and aluminum blocks were separated vertically using Styrofoam. The steel plate and Polyethylene block on the leftmost structure was held in place using the aluminum T-Slot rails supporting the conveyor belt. The flat aluminum plate on the leftmost structure rested on foam blocks on the conveyor belt, and the angled plate rested on the flat aluminum and steel plates. (b) Image reconstruction, experimental GMT scan. (c) Simulated scan. Imaging volume is a 6cm thick slice whose bottom is coincident with the surface of a 49mm foam layer placed on the conveyor belt. Images shown were reconstructed using BPF algorithm.

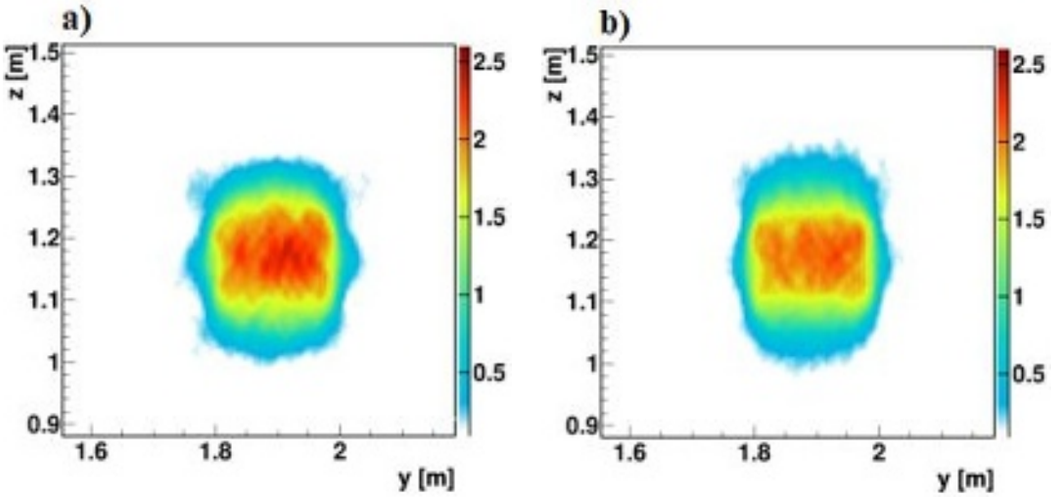

Figure 9. Scan 2 lead bricks imaging in a vertical plane. (a) experimental data, (b) simulated data. The images were reconstructed using the BPF algorithm.

Figure 10 shows the sample geometry and imaging results of Scan 3 in which two brass cubes with dimensions 5.35 × 5.1 × 5.1 cm are enclosed inside an arrangement of aluminum plates. While in both the simulated and experimental imaging results all components of the sample are clearly visible, the contrast in the simulation is slightly higher and exhibits a lower noise level.

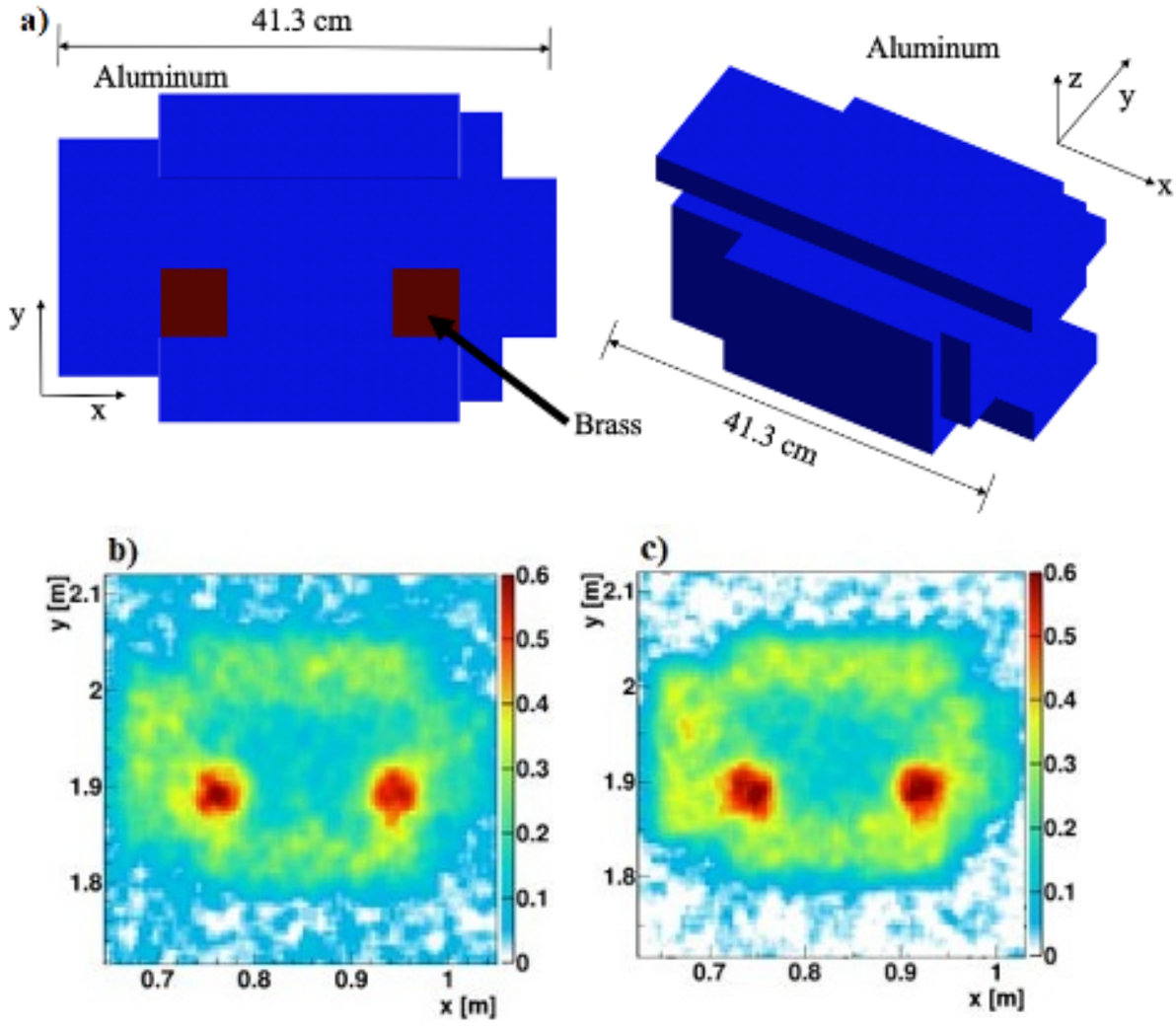

Figure 10. Scan 3 sample geometry and imaging results. (a) CAD rendering of sample geometry**.** Sample constructed using blocks of aluminum and brass in a self-supporting manner. (b) Image reconstruction, experimental GMT scan. (c) Simulated scan. Imaging volume is 6cm thick slice whose bottom is coincident with the surface of a 49mm foam layer placed on the conveyor belt. Images shown were reconstructed using BPF algorithm.

Figure 11 shows the sample geometry and imaging results of Scan 4 along a vertical plane, in order to evaluate the vertical resolution of the GMT and reconstruction algorithms. In this scan, aluminum and lead blocks were arranged in different vertical positions with lead blocks separated by blocks of aluminum and Styrofoam. Image reconstructions show that the two metals are clearly identified in both the simulated and experimental data. Small differences in the image contrast, however, can be seen between simulated and experimental results.

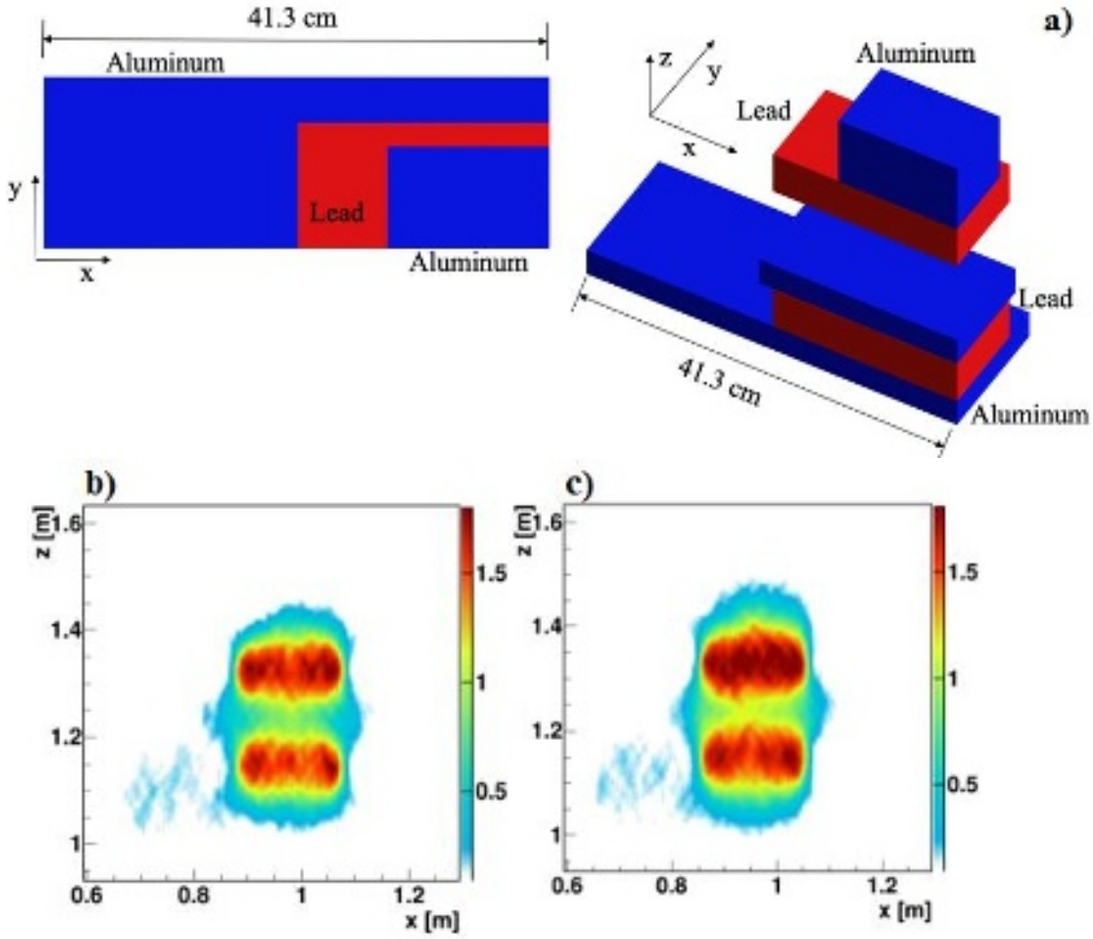

Figure 11. Scan 4 sample geometry and imaging results. (a) CAD rendering of sample geometry**.** Image on left shows top-down perspective while right perspective is rotated to show important detail. Vertical separation between blocks and was done using Styrofoam. Sample constructed using blocks of aluminum and lead. (b) Image reconstruction, experimental GMT scan. (c) Simulated scan. Imaging volume is 6cm thick slice between is 184 and 190 cm along the short horizontal axis of the scanner. Images shown were reconstructed using BPF algorithm.

Figure 12 shows the image reconstruction done for the Scan 4 sample (Fig. 11a) using the PoCA algorithm. The vertical separation is much less clear when the PoCA algorithm is used in the reconstruction when compared with the BPF algorithm, Fig. 11. The fundamental difference between these two image reconstruction methods is that the PoCA image reconstruction algorithm approximated the multiple scattering into a single scattering point, while the BPF image reconstruction algorithm includes an explicit treatment for the multiple scattering effect.

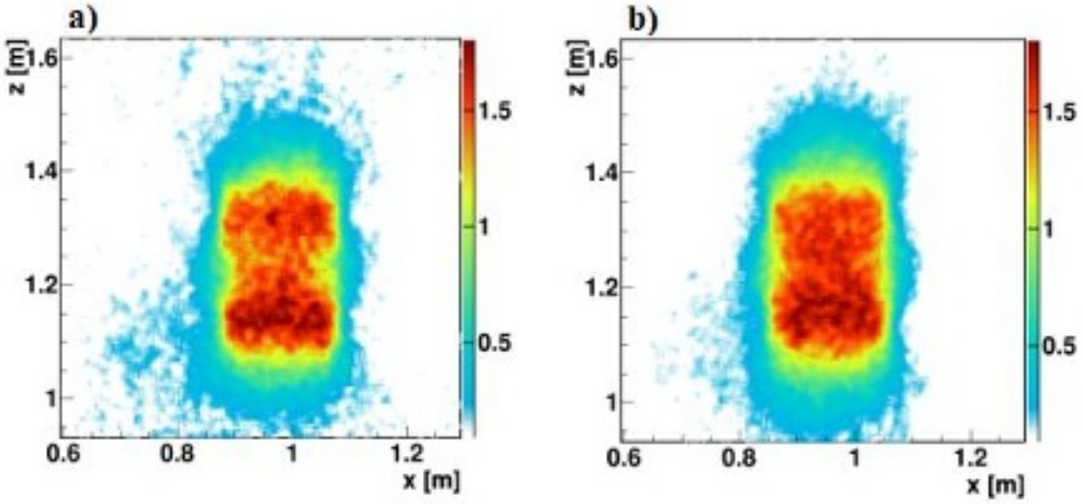

Figure 12. Scan 4 imaging results using PoCA algorithm. (a) Image reconstruction, experimental GMT scan. (b) Simulated scan. Imaging volume is 6cm thick slice between is 184 and 190 cm along the short horizontal axis of the scanner. Image reconstructions were done using the same experimental and simulation data as Fig. 11.

The images in Figs. 7-12 created using experimental data feature slightly more noise than the images created using simulated data. In the Geant4 simulations, however, the GMT was modeled with all drift tubes functioning, while several readout channels in the GMT are faulty. Figures 13 and 14 show the distribution of experimentally measured muon tracks' intersections with the drift tubes in the top and bottom (Fig. 13), left and right (Fig. 14) supermodules. These figures are the transmission images of the tubes in the supermodule. The hit counts in the images can be directly linked to the tube efficiencies, where a low hit count in the image means low efficiency at the corresponding tube. The figures clearly show several faulty readout channels in all supermodules, which reduces the overall performance of the GMT.

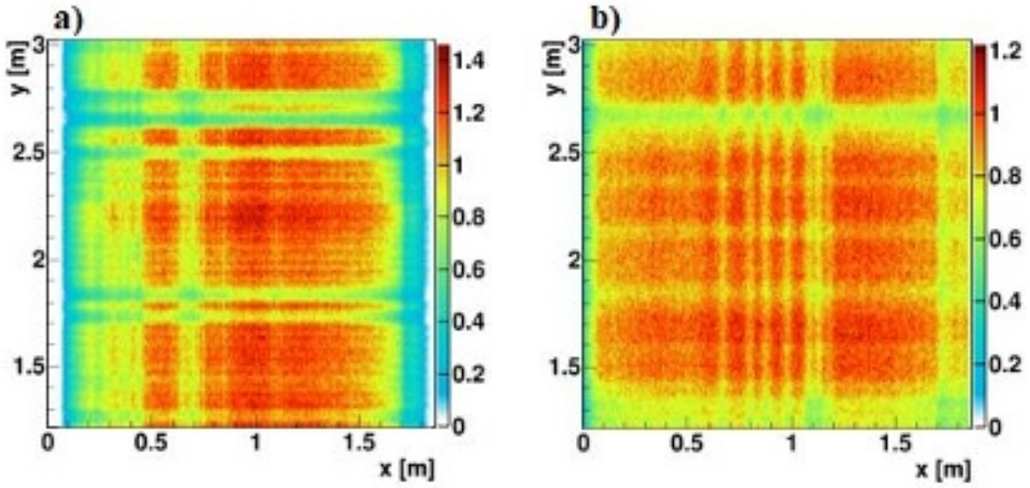

Figure 13. GMT Scanner Muon Hit Counts on Top and Bottom Supermodules. (a) Top supermodule (b) bottom supermodule. Data from the empty scanner run are shown. Hit counts are integrated in the vertical (out of page) direction.

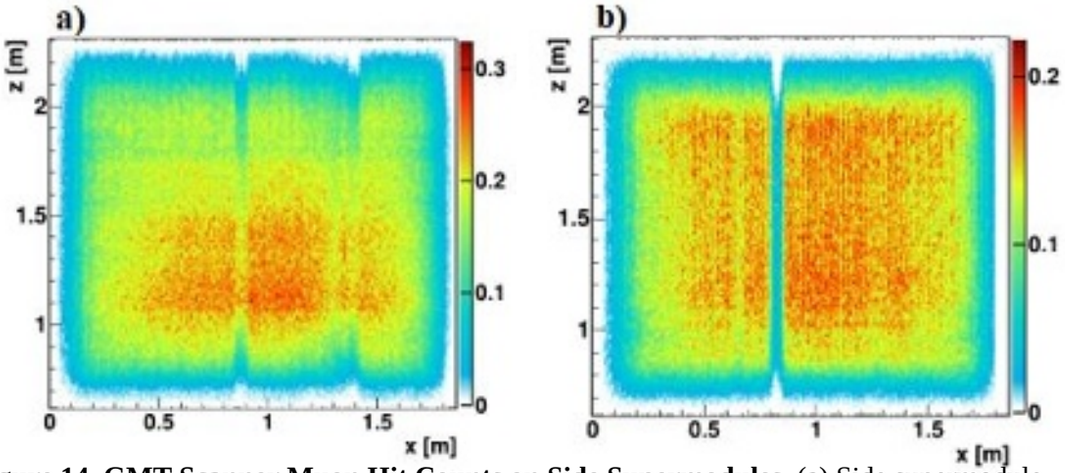

Figure 14. GMT Scanner Muon Hit Counts on Side Supermodules. (a) Side supermodule, imaging plane at y = 38.9cm. (b) Side supermodule, imaging plane at y = 388.5cm. Data from the empty scanner run are shown. Hit counts are integrated in the y-direction.

4. Conclusions.

The first sets of experimental measurements using the Giant Muon Tracker at the Los Alamos National Laboratory were successfully performed. A variety of materials in several configurations were placed inside the GMT and imaged for 48 hours using cosmic ray muons. A simulation suite for the GMT was developed and the imaging results reconstructed from experimental and simulated data were compared, showing excellent agreement. Small inconsistencies between simulated and experimental reconstructions can be attributed to several possible factors, the most significant being the faulty readout channels shown in Figs. 13, 14. A more faithful simulation can be done by removing drift tube hits from the simulation where they correspond to the faulty channels in the GMT. Additionally, the simulation uses a muon source whose energy and zenith angle distributions are likely to be slightly different from those that would be experimentally measured. The simulation of the GMT models only the supermodules and samples, without accounting for materials surrounding the GMT that could affect the muon source distribution. The supermodules are held in place using a thick steel frame (Fig. 2), while electric supply boxes and network hardware

are attached to the frame next to the side supermodules. The simulation also does not account for the possibility that the incoming muons' distribution is affected by the materials out of which the LANL staging area building is constructed. The accuracy of the experimentally measured source distribution, however, is limited by the GMT's inherent precision and faulty readout channels. This complicates the extent to which meaningful conclusions can be drawn regarding the accuracy of the simulated source distribution relative to the experimentally measured distribution.

Because the GMT has been kept in storage for several years, some of the gas from the drift tubes has leaked which is causing a reduction in the scanner's angular resolution by an approximate factor of two. Solutions for mitigating this are being explored, including performing a recalibration of the scanner with the drift tube voltages increased. Additional data will be taken when the scanner's resolution has been restored and used to update the variance imposed on the drift radii calculated in the simulation. This should lead to a significant improvement in the performance of the GMT. Refilling the gas in the tubes is also an option if the increased voltage does not meaningfully improve resolution, or if further degradation occurs.

Despite the above limitations, the simulation suite developed as part of this work will be of significant utility to future studies using the GMT. Although the four supermodules of the GMT are designed to be moved independently, doing this is a time-consuming process with risk of causing damage to equipment and injury to personnel. Performing measurements can also take days to weeks depending on the properties of the sample as well as supermodule placement and muon source strength in certain contexts like underground or underwater measurements. Optimizing experimental setups can be done safely and rapidly using reduced order simulation models to estimate the results that can be expected under a variety of external conditions, sample configurations and supermodule placement. The Geant4 simulation suite described in this work can be used to validate these reduced order models without relying on experimental data. This is especially important as the GMT is planned to be used for imaging spent nuclear fuel casks outdoors in the presence of radiation. Optimal placement of the supermodules is crucial to minimize the needed imaging time and avoid radiation damage to the GMT. The simulation suite will also be complementary to physical alignment studies that will need to be done every time the relative position of the four supermodules changes.

5. Acknowledgments. This work was supported by DOE-NEUP grant 21-24292. This research is partially based upon work supported by the Department of Energy/National Nuclear Security Administration under Award Number DE-NA0004008.

6. Author Contributions. Conceptualization, A.O.; methodology: A.O., G.Y., R.K., C.L.M.; software, A.O., G.Y., D.A., E.G.; validation, A.O., G.Y.; experimental setup and data taking: J.S., D.P., E.G., J.M.D., S.V., C.L.M.; visualization: G.Y., J.S., S.H., J.M.D., C.L.M., A.O.; formal analysis, G.Y., A.O.; data curation, A.O., G.Y.; writing – original draft preparation, A.O., G.Y.; writing – review and editing, G.Y., J.S., D.P., E.G., J.M.D., S.V., S.H., D.A., K.S., C.L.M., R.K., A.O.; supervision, S.V., K.S., C.L.M., A.O.; funding acquisition, A.O., G.Y., R.K., C.L.M., K.S.; project administration, A.O. All authors have read and agreed to the current version of the manuscript.

7. Conflict of Interest Statement. C.L.M. receives income from several patents on muon tomography that are licensed by the Los Alamos National Laboratory to Decision Sciences Corporation. R.K. is a founder and shareholder of Lynkeos Technology Ltd. in the United Kingdom but has no active role in the company. The remaining authors declare no conflicts of interest to disclose.

8. Data Availability Statement. *The data that support the findings of this study are available from the corresponding author upon reasonable request.*

9. References

[1] K. A. Olive, "Review of Particle Physics," *Chin. Phys. C*, vol. 38, no. 9, p. 090001, Aug. 2014, doi: 10.1088/1674-1137/38/9/090001.
[2] H. K. M. Tanaka *et al.*, "Three-dimensional computational axial tomography scan of a volcano with cosmic ray muon radiography," *J. Geophys. Res.*, vol. 115, no. B12, p. B12332, Dec. 2010, doi: 10.1029/2010JB007677.
[3] E. Guardincerri *et al.*, "3D Cosmic Ray Muon Tomography from an Underground Tunnel," *Pure Appl. Geophys.*, vol. 174, no. 5, pp. 2133–2141, May 2017, doi: 10.1007/s00024-017-1526-x.
[4] K. N. Borozdin *et al.*, "Radiographic imaging with cosmic-ray muons," *Nature*, vol. 422, no. 6929, Art. no. 6929, Mar. 2003, doi: 10.1038/422277a.
[5] W. C. Priedhorsky *et al.*, "Detection of high-Z objects using multiple scattering of cosmic ray muons," *Rev. Sci. Instrum.*, vol. 74, no. 10, pp. 4294–4297, Oct. 2003, doi: 10.1063/1.1606536.
[6] C. L. MORRIS *et al.*, "Tomographic Imaging with Cosmic Ray Muons," *Sci. Glob. Secur.*, vol. 16, no. 1–2, pp. 37–53, Oct. 2008, doi: 10.1080/08929880802335758.
[7] E. Guardincerri *et al.*, "Imaging the dome of Santa Maria del Fiore using cosmic rays," *Philos. Trans. R. Soc. Math. Phys. Eng. Sci.*, vol. 377, no. 2137, p. 20180136, Jan. 2019, doi: 10.1098/rsta.2018.0136.
[8] J. Perry *et al.*, "Imaging a nuclear reactor using cosmic ray muons," *J. Appl. Phys.*, vol. 113, no. 18, p. 184909, May 2013, doi: 10.1063/1.4804660.
[9] J. M. Durham *et al.*, "Tests of cosmic ray radiography for power industry applications," *AIP Adv.*, vol. 5, no. 6, p. 067111, Jun. 2015, doi: 10.1063/1.4922006.
[10] J. M. Durham *et al.*, "Verification of Spent Nuclear Fuel in Sealed Dry Storage Casks via Measurements of Cosmic-Ray Muon Scattering," *Phys. Rev. Appl.*, vol. 9, no. 4, p. 044013, Apr. 2018, doi: 10.1103/PhysRevApplied.9.044013.
[11] D. Poulson *et al.*, "Cosmic ray muon computed tomography of spent nuclear fuel in dry storage casks," *Nucl. Instrum. Methods Phys. Res. Sect. Accel. Spectrometers Detect. Assoc. Equip.*, vol. 842, pp. 48–53, Jan. 2017, doi: 10.1016/j.nima.2016.10.040.
[12] D. Poulson, J. Bacon, M. Durham, E. Guardincerri, C. L. Morris, and H. R. Trellue, "Application of muon tomography to fuel cask monitoring," *Philos. Trans. R. Soc. Math. Phys. Eng. Sci.*, vol. 377, no. 2137, p. 20180052, Jan. 2019, doi: 10.1098/rsta.2018.0052.
[13] D. F. Mahon *et al.*, "A prototype scintillating-fibre tracker for the cosmic-ray muon tomography of legacy nuclear waste containers," *Nucl. Instrum. Methods Phys. Res. Sect. Accel. Spectrometers Detect. Assoc. Equip.*, vol. 732, pp. 408–411, Dec. 2013, doi: 10.1016/j.nima.2013.05.119.
[14] T. J. Stocki *et al.*, "Machine learning for the cosmic ray inspection and passive tomography project (CRIPT)," in *2012 IEEE Nuclear Science Symposium and Medical Imaging Conference Record (NSS/MIC)*, Anaheim, CA: IEEE, Oct. 2012, pp. 91–94. doi: 10.1109/NSSMIC.2012.6551067.

[15] F. Riggi *et al.*, "The Muon Portal Project: Commissioning of the full detector and first results," *Nucl. Instrum. Methods Phys. Res. Sect. Accel. Spectrometers Detect. Assoc. Equip.*, vol. 912, pp. 16–19, Dec. 2018, doi: 10.1016/j.nima.2017.10.006.

[16] S. Barnes *et al.*, "Cosmic-Ray Tomography for Border Security," *Instruments*, vol. 7, no. 1, p. 13, Mar. 2023, doi: 10.3390/instruments7010013.

[17] P. Checchia, "Review of possible applications of cosmic muon tomography," *J. Instrum.*, vol. 11, no. 12, pp. C12072–C12072, Dec. 2016, doi: 10.1088/1748-0221/11/12/C12072.

[18] S. Procureur, "Muon imaging: Principles, technologies and applications," *Nucl. Instrum. Methods Phys. Res. Sect. Accel. Spectrometers Detect. Assoc. Equip.*, vol. 878, pp. 169–179, Jan. 2018, doi: 10.1016/j.nima.2017.08.004.

[19] S. Agostinelli *et al.*, "Geant4—a simulation toolkit," *Nucl. Instrum. Methods Phys. Res. Sect. Accel. Spectrometers Detect. Assoc. Equip.*, vol. 506, no. 3, pp. 250–303, Jul. 2003, doi: 10.1016/S0168-9002(03)01368-8.

[20] "Least Absolute Deviation Regression," in *The Concise Encyclopedia of Statistics*, New York, NY: Springer New York, 2008, pp. 299–302. doi: 10.1007/978-0-387-32833-1_225.

[21] H. A. Bethe, "Molière's Theory of Multiple Scattering," *Phys. Rev.*, vol. 89, no. 6, pp. 1256–1266, Mar. 1953, doi: 10.1103/PhysRev.89.1256.

[22] S. Goudsmit and J. L. Saunderson, "Multiple Scattering of Electrons," *Phys. Rev.*, vol. 57, no. 1, pp. 24–29, Jan. 1940, doi: 10.1103/PhysRev.57.24.

[23] H. W. Lewis, "Multiple Scattering in an Infinite Medium," *Phys. Rev.*, vol. 78, no. 5, pp. 526–529, Jun. 1950, doi: 10.1103/PhysRev.78.526.

[24] B. Rossi and K. Greisen, "Cosmic-Ray Theory," *Rev. Mod. Phys.*, vol. 13, no. 4, pp. 240–309, Oct. 1941, doi: 10.1103/RevModPhys.13.240.

[25] S. Eidelman *et al.*, "Review of Particle Physics," *Phys. Lett. B*, vol. 592, no. 1–4, pp. 1–5, Jul. 2004, doi: 10.1016/j.physletb.2004.06.001.

[26] R. Brun and F. Rademakers, "ROOT — An object oriented data analysis framework," *Nucl. Instrum. Methods Phys. Res. Sect. Accel. Spectrometers Detect. Assoc. Equip.*, vol. 389, no. 1–2, pp. 81–86, Apr. 1997, doi: 10.1016/S0168-9002(97)00048-X.

[27] C. Hagmann, D. Lange, J. Verbeke, and D. Wright, "Cosmic-ray Shower Library (CRY), UCRL-TM-229453." Lawrence Livermore National Laboratory, Mar. 24, 2012. [Online]. Available: https://nuclear.llnl.gov/simulations/doc_cry_v1.7/cry.pdf

[28] V. Ivanchenko *et al.*, "Progress of Geant4 electromagnetic physics developments and applications," *EPJ Web Conf.*, vol. 214, p. 02046, 2019, doi: 10.1051/epjconf/201921402046.

[29] V. N. Ivanchenko, O. Kadri, M. Maire, and L. Urban, "Geant4 models for simulation of multiple scattering," *J. Phys. Conf. Ser.*, vol. 219, no. 3, p. 032045, Apr. 2010, doi: 10.1088/1742-6596/219/3/032045.

[30] G. Chu and K.-C. Tam, "Three-dimensional imaging in the positron camera using Fourier techniques," *Phys. Med. Biol.*, vol. 22, no. 2, p. 245, Mar. 1977, doi: 10.1088/0031-9155/22/2/005.

[31] L. J. Schultz, *Cosmic ray muon radiography*. Portland State University, 2003.

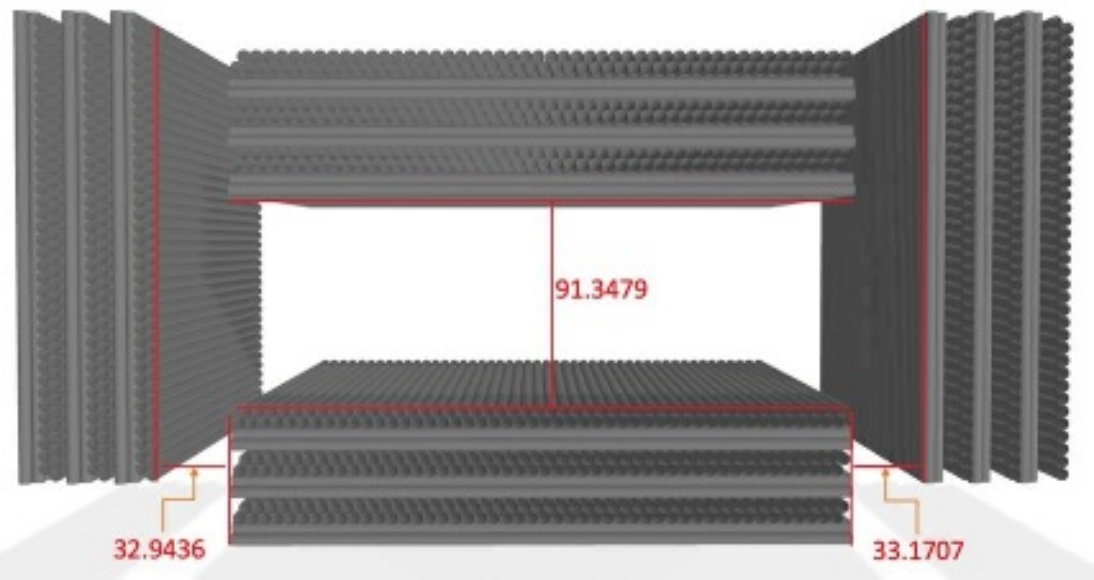
91.3479
32.9436
33.1707

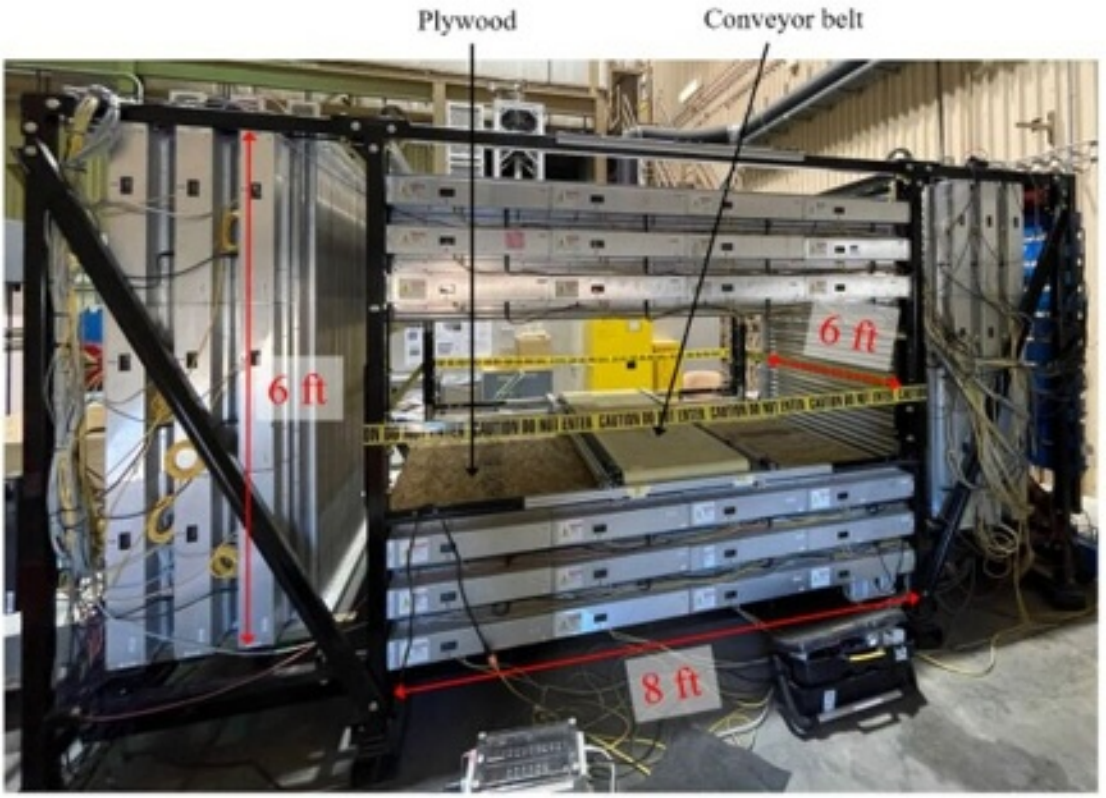
Plywood
Conveyor belt
6 ft
6 ft
8 ft

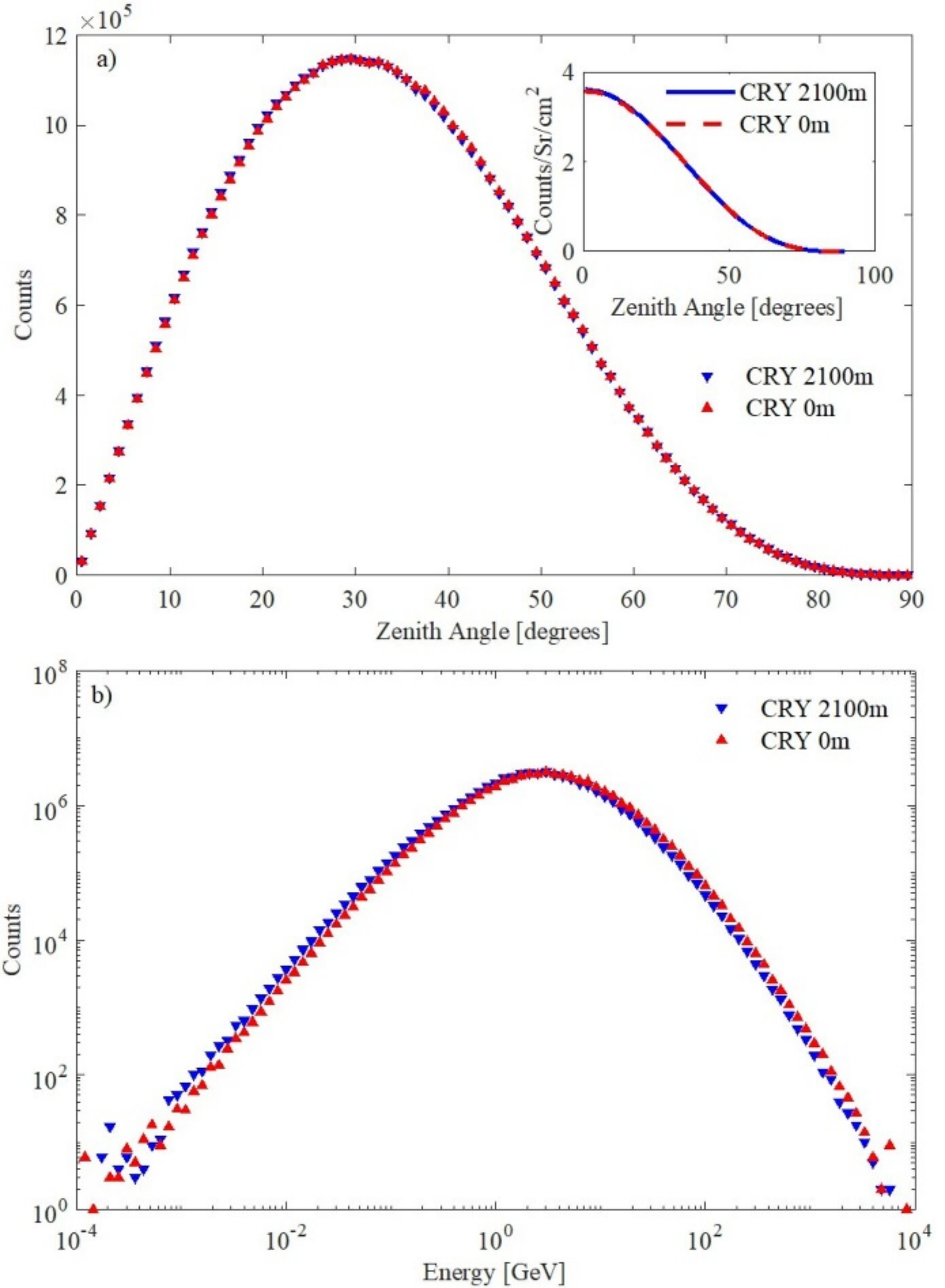
a)
×10^5
Counts
Zenith Angle [degrees]
CRY 2100m
CRY 0m
Counts/Sr/cm^2
Zenith Angle [degrees]
CRY 2100m
CRY 0m
b)
Counts
Energy [GeV]
CRY 2100m
CRY 0m

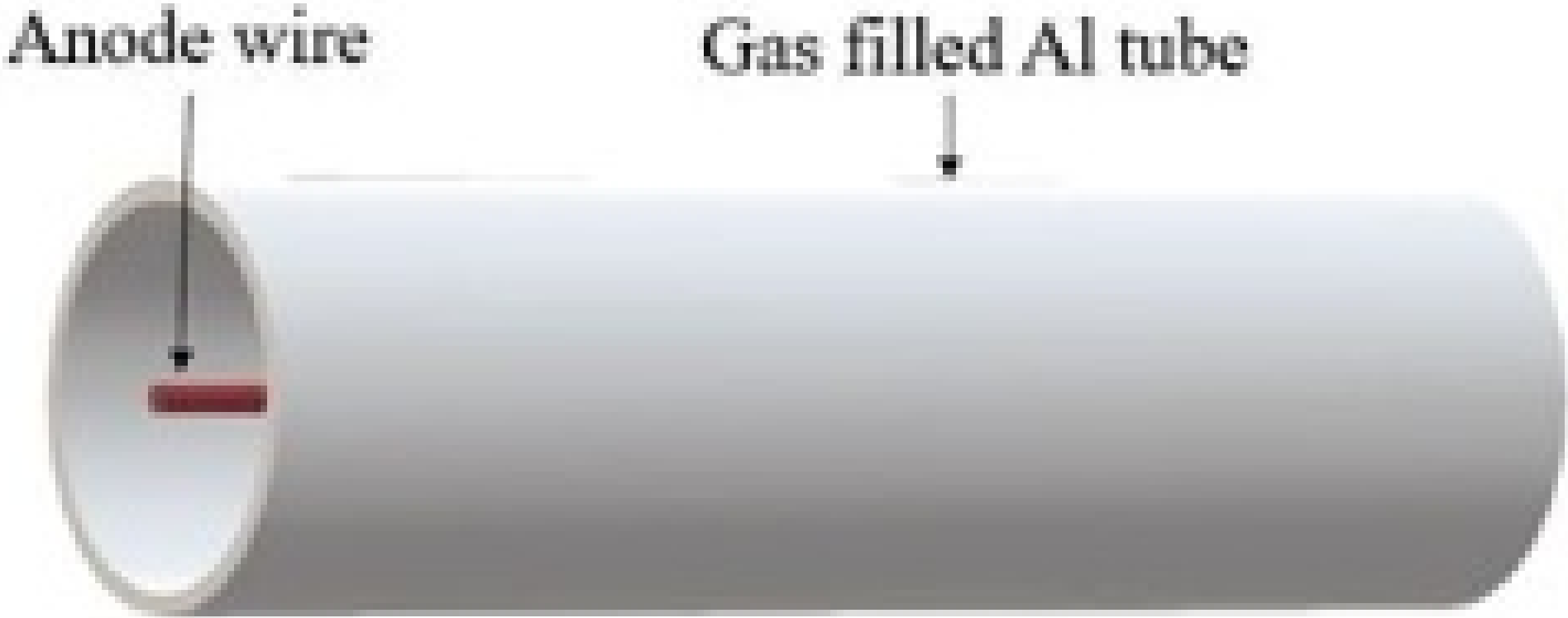
Anode wire
Gas filled Al tube

Ideal Simulation Model
Multiple Scattering
Multiple Scattering + Delta Rays
All Uncertainty Effects Modeled
Experimental Data
Counts
10^6
10^4
10^2
10^0
0
50
100
150
200
250
300
350
400
450
500
Scattering Angle [mrad]

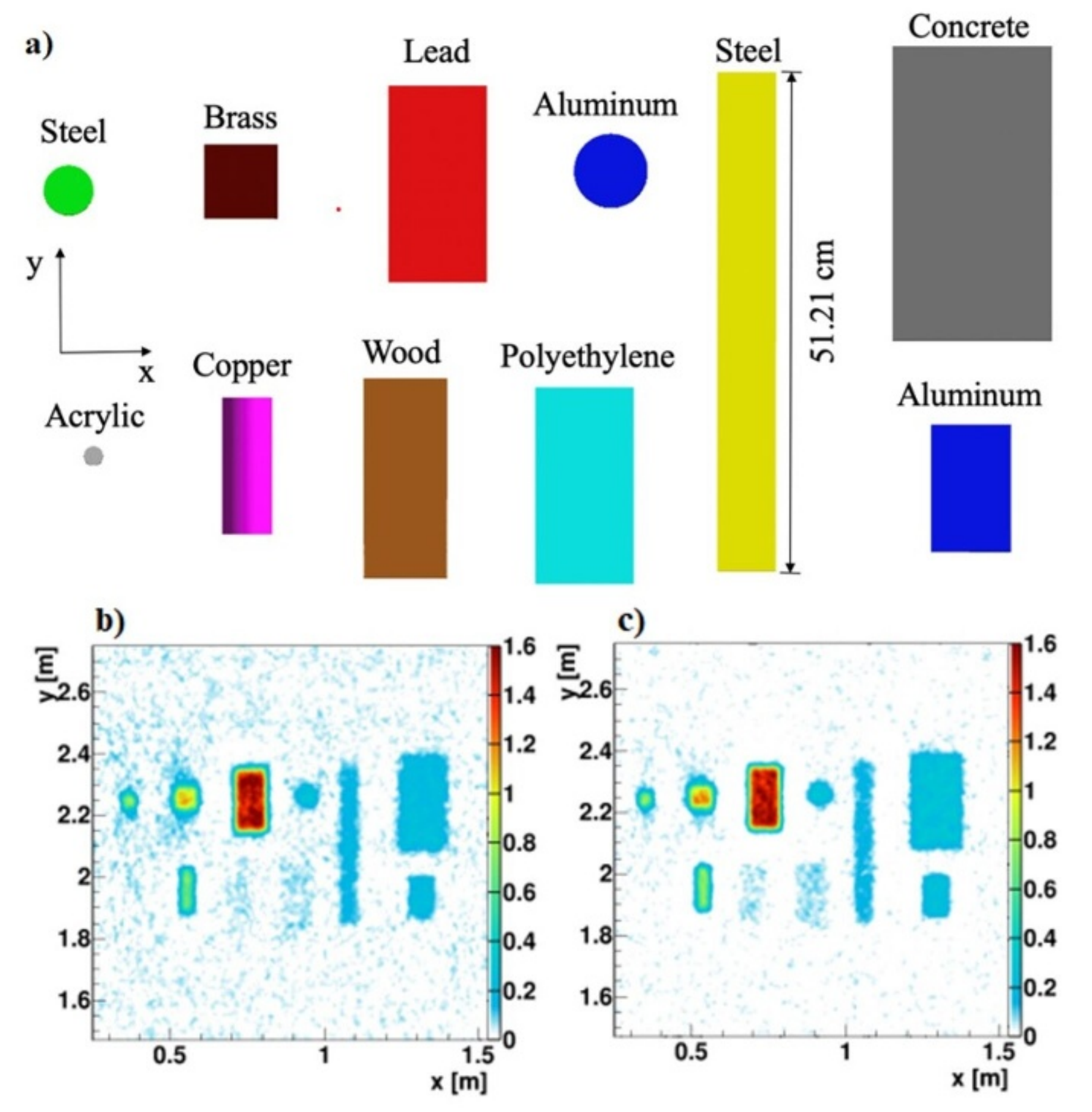
a)
Steel
Brass
Lead
Aluminum
Steel
Concrete
51.21 cm
y
x
Acrylic
Copper
Wood
Polyethylene
Aluminum
b)
c)
y [m]
x [m]
0.5
1
1.5
1.6
1.8
2
2.2
2.4
2.6
0
0.2
0.4
0.6
0.8
1
1.2
1.4
1.6

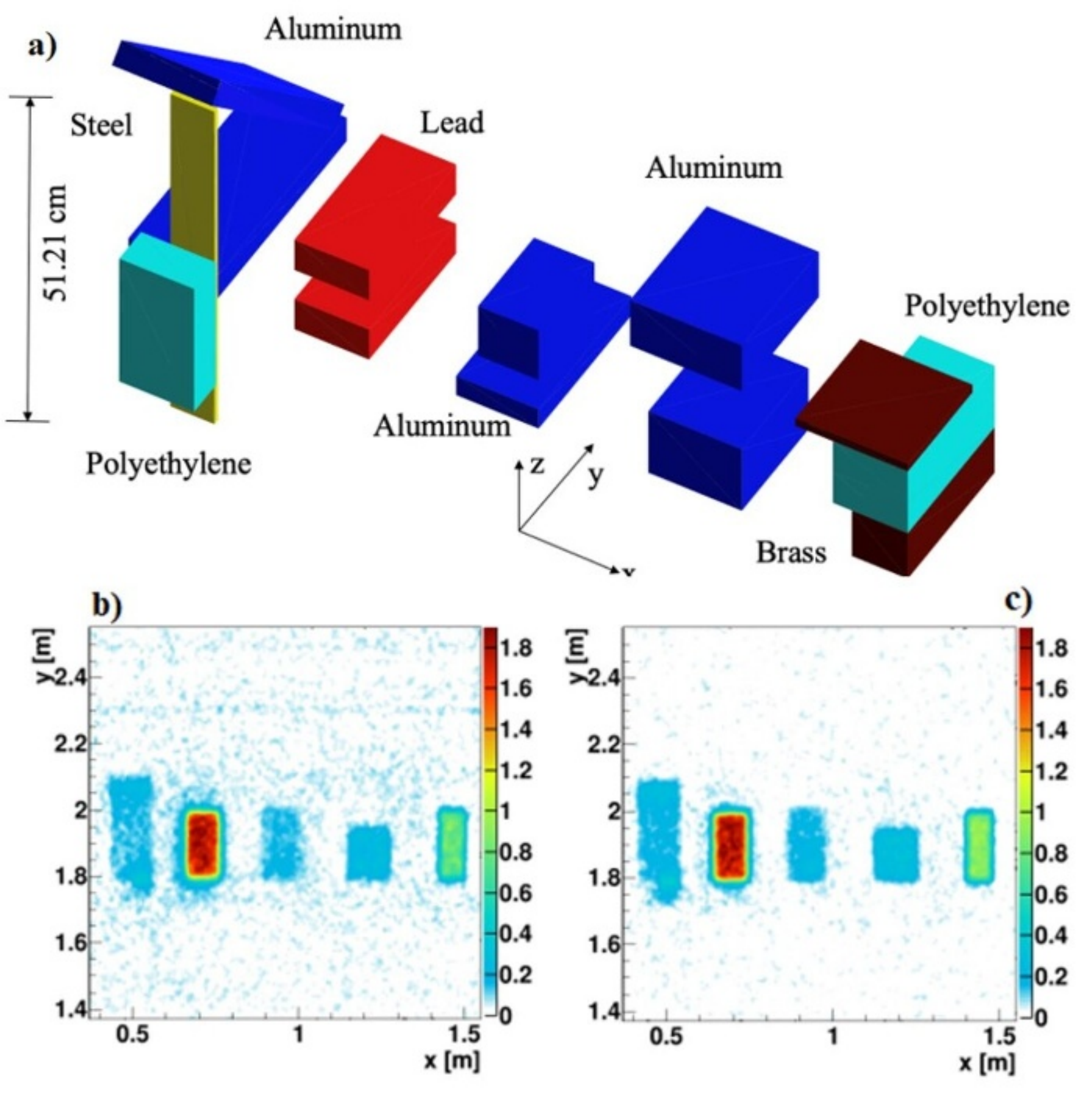
a)
Aluminum
Steel
Lead
Aluminum
51.21 cm
Polyethylene
Aluminum
Polyethylene
z
y
x
Brass
b)
c)
y [m]
x [m]
0.5
1
1.5
1.4
1.6
1.8
2
2.2
2.4
0
0.2
0.4
0.6
0.8
1
1.2
1.4
1.6
1.8

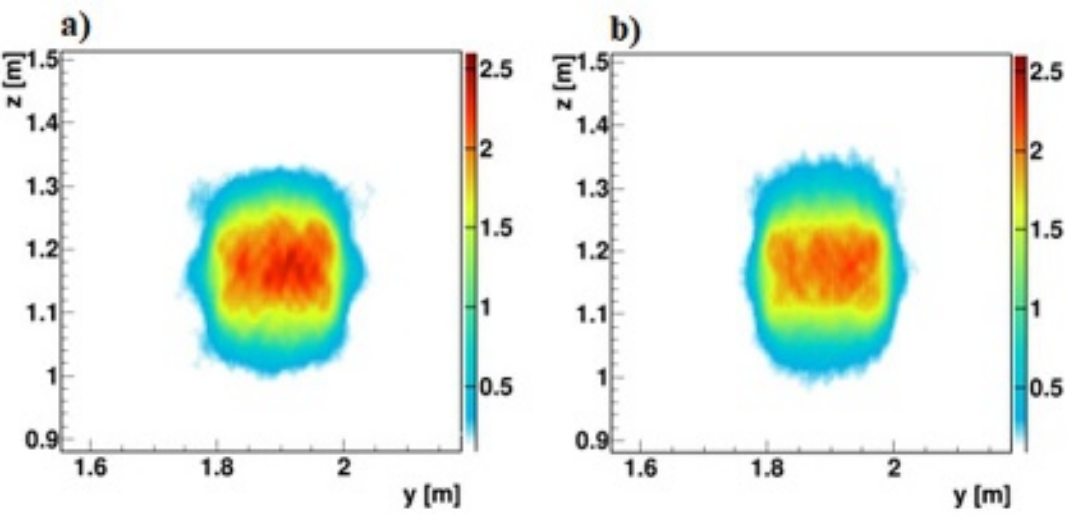
a)
b)
z [m]
y [m]
1.5
1.4
1.3
1.2
1.1
1
0.9
1.6
1.8
2
2.5
2
1.5
1
0.5

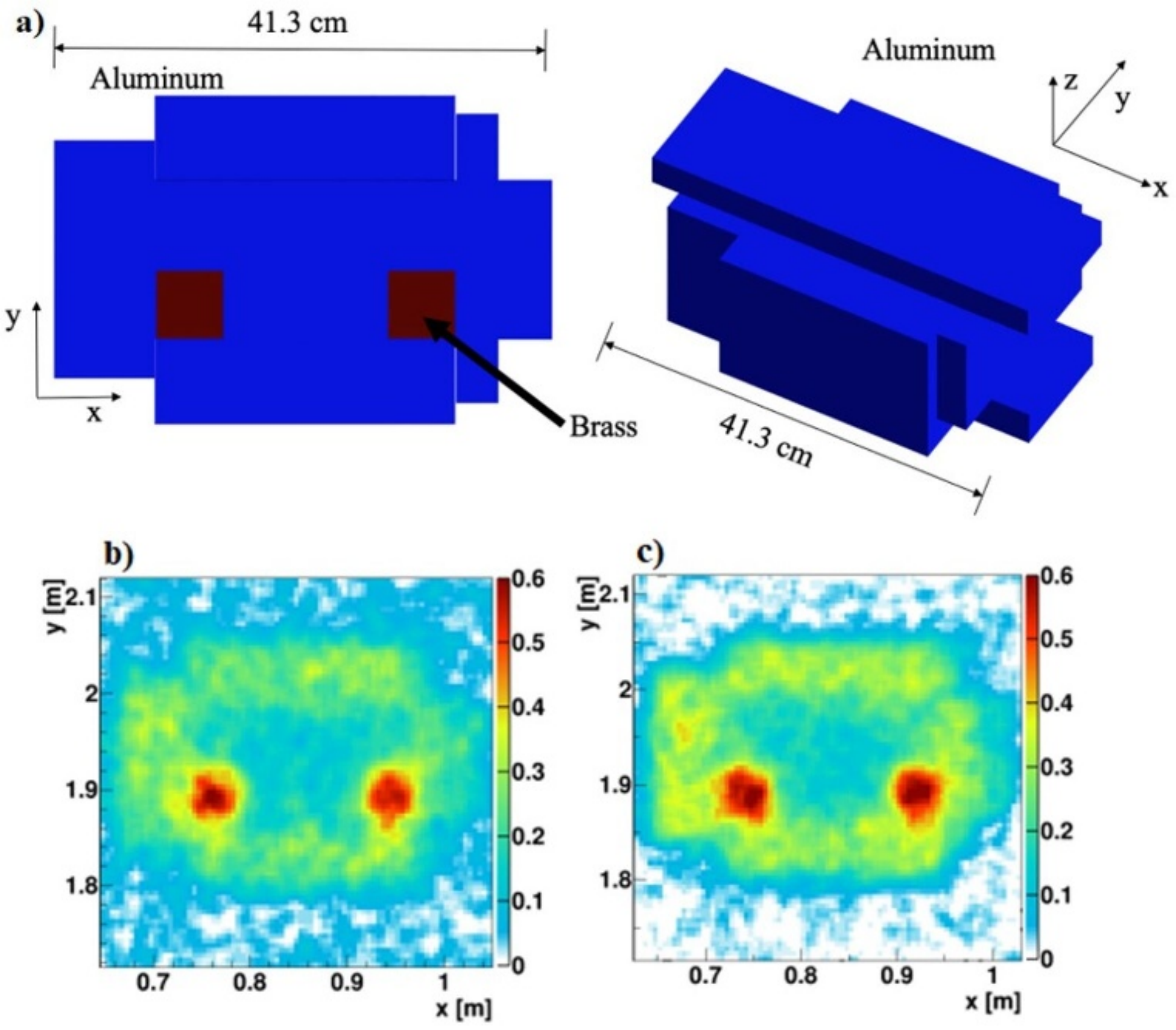
a)
41.3 cm
Aluminum
Aluminum
z
y
x
y
x
Brass
41.3 cm
b)
y [m]
2.1
2
1.9
1.8
0.7
0.8
0.9
1
x [m]
0.6
0.5
0.4
0.3
0.2
0.1
0
c)
y [m]
2.1
2
1.9
1.8
0.7
0.8
0.9
1
x [m]
0.6
0.5
0.4
0.3
0.2
0.1
0

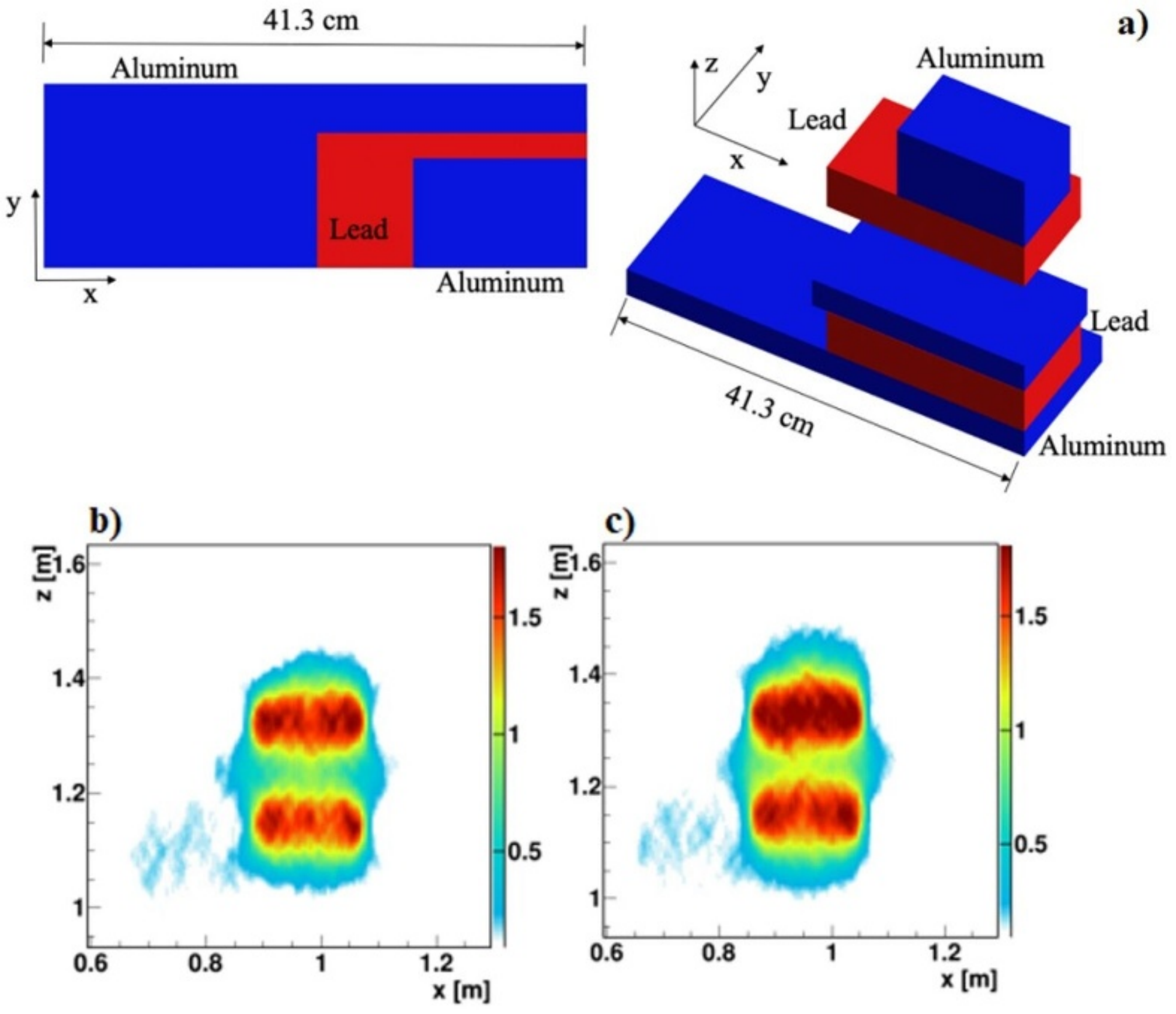
41.3 cm
Aluminum
Lead
Aluminum
y
x
a)
z
y
x
Aluminum
Lead
Lead
41.3 cm
Aluminum
b)
z [m]
1.6
1.4
1.2
1
0.6
0.8
1
1.2
x [m]
1.5
1
0.5
c)
z [m]
1.6
1.4
1.2
1
0.6
0.8
1
1.2
x [m]
1.5
1
0.5

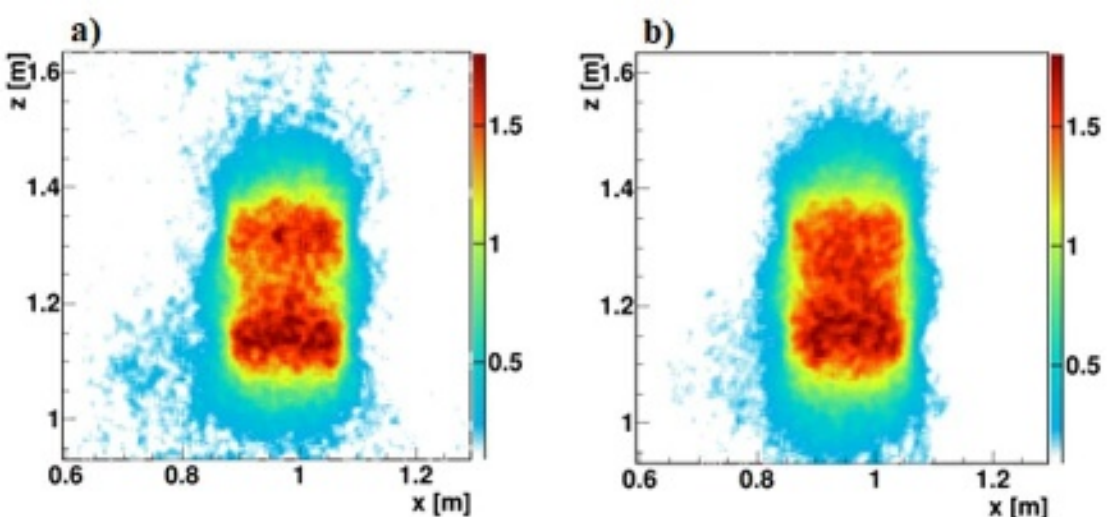
a)
b)
z [m]
x [m]
1.6
1.4
1.2
1
0.6
0.8
1
1.2
1.5
1
0.5

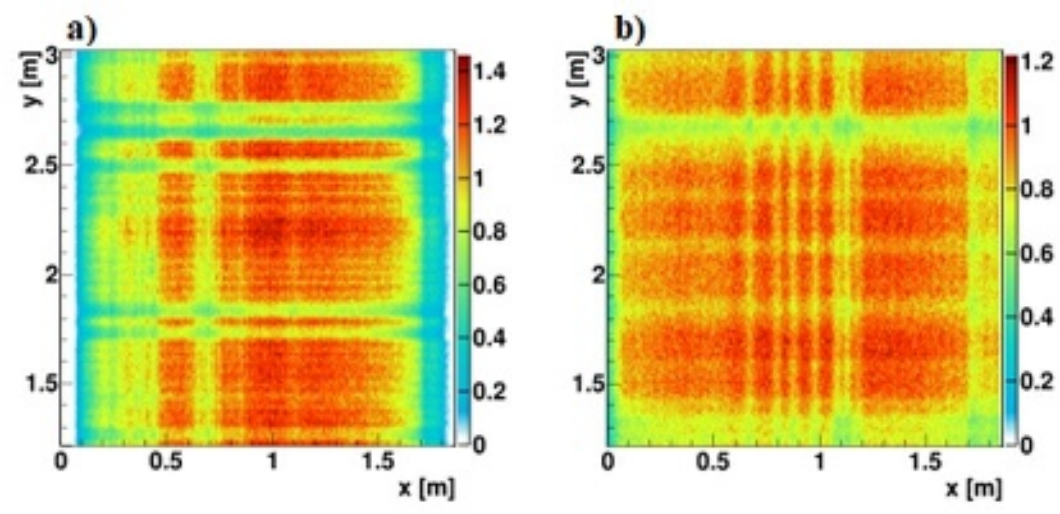
a)
b)
y [m]
x [m]
3
2.5
2
1.5
0
0.5
1
1.5
0.2
0.4
0.6
0.8
1.2
1.4

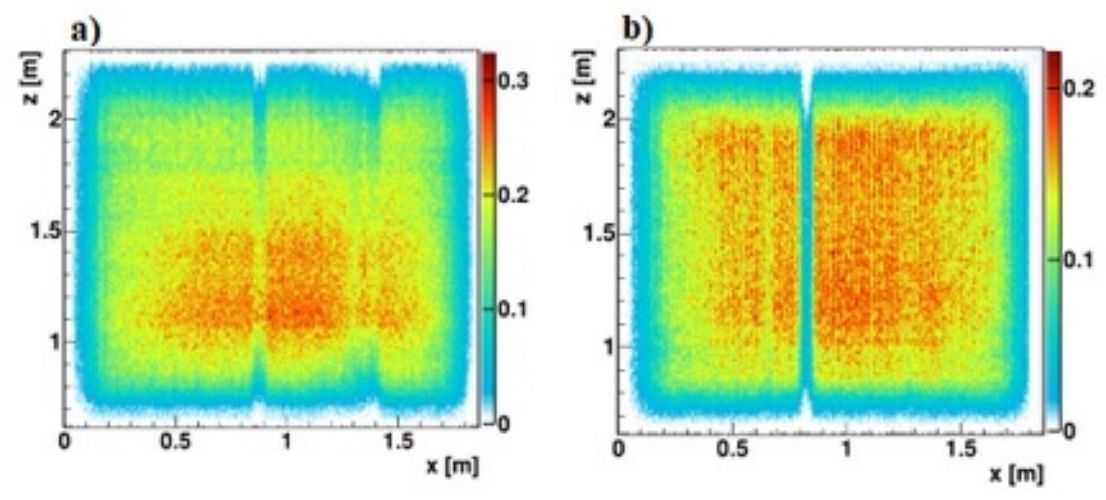
a)
z [m]
2
1.5
1
0
0.5
1
1.5
x [m]
0.3
0.2
0.1
0
b)
z [m]
2
1.5
1
0
0.5
1
1.5
x [m]
0.2
0.1
0